This is the accepted manuscript made available via CHORUS. The article has been published as:

Magnetostriction, Soft Magnetism, and Microwave Properties in Co-Fe-C Alloy Films

Jiawei Wang, Cunzheng Dong, Yuyi Wei, Xianqing Lin, Benson Athey, Yunpeng Chen, Andrew Winter, Gregory M. Stephen, Don Heiman, Yifan He, Huaihao Chen, Xianfeng Liang, Chengju Yu, Yujia Zhang, Elizabeth J. Podlaha-Murphy, Mingmin Zhu, Xinjun Wang, Jun Ni, Michael McConney, John Jones, Michael Page, Krishnamurthy Mahalingam, and Nian X. Sun

Phys. Rev. Applied **12**, 034011 — Published 9 September 2019
DOI: 10.1103/PhysRevApplied.12.034011

Magnetostriction, soft magnetism and microwave properties in Co-Fe-C alloy films

Jiawei Wang, [1,2,*] Cunzheng Dong,[2] Yuyi Wei,[2] Xianqing Lin,[1] Benson Athey,[3] Yunpeng Chen,[4] Andrew Winter,[5] Gregory M. Stephen,[5] Don Heiman,[5] Yifan He,[2] Huaihao Chen,[2] Xianfeng Liang,[2] Chengju Yu[2], Yujia Zhang,[6] Elizabeth J. Podlaha-Murphy,[6] Mingmin Zhu,[2,7] Xinjun Wang,[2] Jun Ni,[8] Michael McConney,[3] John Jones,[3] Michael Page,[3] Krishnamurthy Mahalingam,[3] and Nian X. Sun[2,†]

[1]College of Science, Zhejiang University of Technology, Hangzhou, 310023, China

[2]Department of Electrical and Computer Engineering, Northeastern University, Boston, Massachusetts 02115, USA

[3]Air Force Research Laboratory, Wright-Patterson AFB, Ohio, 45433, USA

[4]Winchester Technologies, LLC, Burlington, Massachusetts 01803, USA

[5]Department of Physics, Northeastern University, Boston, Massachusetts 02115, USA

[6]Department of Chemical and Biomolecular Engineering, Clarkson University, Potsdam, New York 13699, USA

[7]Key Laboratory of Electromagnetic Wave Information Technology and Metrology of Zhejiang Province, College of Information Engineering, China Jiliang University, Hangzhou, 310018, China

[8]State Key Laboratory of Low-Dimensional Quantum Physics and Collaborative Innovation Center of Quantum Matter, Department of Physics, Tsinghua University, Beijing 100084, China

In the past decades, ferromagnet-metalloid alloy films of Co-Fe-B have been widely used in new magnetic devices due to their excellent performance, such as easy industrial-scale fabrication, and considerable ability for tunneling magnetoresistance and perpendicular magnetic anisotropy. However, the insufficient thermal tolerance and interfacial state

densities in the typical CoFeB/MgO system limits devices optimization. Because of the improvement in thermal stability and interfacial properties by carbon element replacement, new theoretical and experimental work on Co-Fe-C alloy film properties have been reported. Here, we report on the magnetostrictive behavior, soft magnetism and microwave properties of a series of $(Co_{0.5}Fe_{0.5})_xC_{1-x}$ films grown on silicon (001) substrates. The addition of carbon changes the Co-Fe-C films from nanocrystalline *bcc* to an amorphous phase and leads to a high saturated magnetostriction constant of 75 ppm, high piezomagnetic coefficient of 10.3 ppm/Oe, excellent magnetic softness with a low coercivity less than 2 Oe, narrow ferromagnetic resonance linewidth of 25 Oe at X-band, extremely low Gilbert damping of 0.002 and up to 500℃ thermal stability. The large saturated magnetostriction constant and piezomagnetic coefficient result from co-existence of nanocrystalline *bcc* and amorphous phases. The extremely low Gilbert damping is related to the minimized density of states around Fermi energy of the alloys induced by carbon doping. The combination of these properties makes Co-Fe-C films a promising candidate to be widely used in voltage tunable magnetoelectric devices and microwave magnetic devices.

*wangjiawei@zjut.edu.cn

†n.sun@northeastern.edu

I. INTRODUCTION

In recent decades, the development of new magnetic devices such as spin-transfer-torque random-access memory (STT-RAM) or spin-torque oscillators [1,2], requires the magnetic properties of each layer to be precisely tuned according to the specifics of the application. The traditional ferromagnetic metals Fe, Co and Ni have large ferromagnetic moments and can be easily fabricated as bulk or films with high purity. However, they have rigid magnetic 3d electron occupation and electronic band structure, which make them difficult to be tuned except by extreme avenues such as considerably large electric field [3,4]. So the modulation of magnetic properties of these materials is limited. This problem can be solved in binary alloy systems. For example, in the Ni_xFe_{1-x} and Co_xFe_{1-x} alloy systems, transitions occur from a body-centered-cubic (*bcc*) to a face-centered-cubic (*fcc*) phase. Such phase transitions result in a nontrivial change in the electronic band structure, which can be seen as additional features in the Slater-Pauling curve [5,6]. Besides, extraordinary behaviors can be achieved around the phase boundary, such as giant magnetostriction as large as 260 ppm observed in textured Co_xFe_{1-x} system [7].

The conventional binary alloys of Ni_xCo_{1-x}, Ni_xFe_{1-x}, and Co_xFe_{1-x} were thoroughly investigated in bulk samples during the 1960s and 1970s [8-10]. But many emerging technologies require films of these materials. Industrial-scale fabrication of magnetic devices requires homogeneous thin-film growth over large surface areas via magnetron sputtering. It has been found that doping metalloid elements into a binary alloy matrix is superior to simple binary alloys in forming smooth layers over large areas [11,12]. The light elements such as B, Si, and N often break down the crystalline phase of binary alloys, forming uniform amorphous structure [13]. A successful case was the ferromagnet-metalloid alloy Co-Fe-B because of its perfect soft ferromagnetism [14] without

magnetocrystalline anisotropy, high spin polarization [15] and considerable large tunneling magnetoresistance (TMR) in magnetic tunnel junctions (MTJs) [16].

To date, Co-Fe-B alloys have been widely used in designing parallel and perpendicular anisotropy MTJs with MgO tunneling barrier. However, the thermal stability of Co-Fe-B alloy film is still a key obstacle. For example, current-induced magnetization switching in the perpendicular anisotropy STT-RAM is of great interest because of its small threshold current density and good thermal stability [17]. But a post-annealing process was necessary to enhance TMR and integrate STT-RAM in perpendicular MTJs design. It was found the perpendicular anisotropy drastically decreased when the annealing temperature was over 350 ℃ [18]. So the perpendicular anisotropy system can only work in limited temperature range for annealing. There have been a few reports on experimental works that the thermal stability of ferromagnetic materials could be effectively improved by doping with carbon atoms. El-Gendy *et al.*'s work showed that the Co-Fe-carbide nanoparticles had larger thermal stability than commonly used materials [19]. Recently, Chen *et al.*'s experiments showed $Co_{0.4}Fe_{0.4}C_{0.2}$ alloy films provided better thermal tolerance, higher perpendicular anisotropy critical thickness and analogous intrinsic damping constant with $Co_{0.4}Fe_{0.4}B_{0.2}$ films [20]. Moreover, the theoretical calculation from Chen *et al.* [21] made the suggestion that C-doped MTJ was predicted to have a significantly higher TMR than the B-doped MTJ due to its higher interfacial state densities in the CoFeX/MgO interface. So the Co-Fe-C alloy is a promising candidate that could be more widely used than the Co-Fe-B alloy. But the magnetic properties of alloys always held to the composition dependent rule. Thus, the composition dependence of the ferromagnetic properties of Co-Fe-C is highly desired.

Because the $Co_{0.4}Fe_{0.4}B_{0.2}$ composition was used in most research regarding its lowest intrinsic damping constant and highest tunneling spin polarization in the Co-Fe-B alloys [15], $(Co_{0.5}Fe_{0.5})_xC_{1-x}$ was chosen in our study due to its compositional similarity. So far, there have been no reports on carbon content (CC) dependent magnetostriction, magnetism and microwave properties in $(Co_{0.5}Fe_{0.5})_xC_{1-x}$ alloy films.

In this paper, we studied magnetostriction, soft magnetism and microwave properties of different CC in a series of $(Co_{0.5}Fe_{0.5})_xC_{1-x}$ films grown on silicon (001) substrate. It was shown that a combination of high saturation magnetostriction constant (λ_s), high piezomangetic coefficient ($d\lambda/dH$), very low coercivity, narrow ferromagnetic resonance (FMR) linewidth, low Gilbert damping constant and high thermal stability have been achieved. The notable result was that λ_s was larger than the value in Ga-Fe-B alloys [22] and 3 times larger than in Co-Fe-B alloys [23]. The minimum in-plane Gilbert damping was 0.002. All of these properties make Co-Fe-C films attractive for voltage tunable magnetoelectric devices in multiferroic composite structures and other microwave magnetic devices.

II. EXPERIMENTAL DETAILS

A. Sample Preparation

Multilayers structures of Ta(5)/$(Co_{0.5}Fe_{0.5})_xC_{1-x}$(20)/Ta(5) (in nm) with various CC were sputtered onto (001)-oriented 6×6 mm^2 silicon substrates using two separate targets of $Co_{0.5}Fe_{0.5}$ and carbon. The Si (001) substrate was natural oxidized with oxide thickness 1-2 nm. The CC of the $(Co_{0.5}Fe_{0.5})_xC_{1-x}$ films was varied by changing the carbon target power while keeping the $Co_{0.5}Fe_{0.5}$ target power at 30 W on the 2 inch diameter targets.

The $(Co_{0.5}Fe_{0.5})_xC_{1-x}$ films were deposited in a 3 mTorr Ar atmosphere in a vacuum chamber with a base pressure better than 1×10^{-7} Torr.

B. Experimental Characterization

The respective deposition rate and the crystal structures were examined by X-ray reflectivity (XRR) and X-ray diffraction (XRD) using a Bruker D8 High-resolution diffractometer with the Cu K_α radiation. The $(Co_{0.5}Fe_{0.5})_xC_{1-x}$ films' compositions were characterized by X-ray photoelectron spectroscopy (XPS) on CMSE's PHI Versaprobe II. Fast Fourier transform (FFT) analysis in the high resolution transmission electron microscope (HRTEM) was employed for $(Co_{0.5}Fe_{0.5})_xC_{1-x}$ films' crystallization nature. Magnetostriction constants were measured using a Si machined cantilevers with the largest drive magnetic field up to 300 Oe and the best resolution of 0.1 ppm. Before measurement, a large magnetic field along the in-plane magnetic easy axis (MEA) was used to saturate the sample. The cantilever's bending was monitored when a AC magnetic field was applied along the in-plane magnetic hard axis (MHA). A standard sample of 100 nm $Ga_{0.176}Fe_{0.704}B_{0.12}$ film with λ_s = 70 ppm [22] was used to calibrate the system (instrument details are introduced in reference [24]). Magnetization versus magnetic field M-H curves were measured using a Quantum Design SQUID Magnetic Properties Measurement System (MPMS) and Vibrating Sample Magnetometer (VSM). Microwave properties were characterized using a homemade broadband apparatus equipped with an adjustable frequency of 0.01-26 GHz FMR spectrometer.

III. RESULTS AND DISCUSSION

A. Structure and composition

XRD and XPS measurements were carried out to characterize the structure and composition of the films. Fig. 1(a) shows that *bcc* (110) reflection from $Co_{0.5}Fe_{0.5}$ can be seen in the Co-Fe-C films with low CC. The signal to noise ratio (SNR) analysis after normalizing the Si substrate (004) reflection in Supplemental Material S1 [25] indicates that the doping carbon atoms in the $Co_{0.5}Fe_{0.5}$ alloy decreases the (110) reflection intensity, leading to refined grain size and more disordered lattice. This result matches what has been observed in Ga-Fe-B and Co-Fe-B films [15, 22]. To characterize films' crystallization nature with CC, rocking curve of (110) reflection was employed as shown in Fig. 1(b). The accurate full width at half maximum (FWHM) was obtained using the Gauss peak function fitting as the dashed curves in Fig. 1(b). The dotted curves were guided to realize the broaden process of FWHM with the CC increase. The FWHM of Co-Fe-C films were collected in Fig. 1(c) as red balls. The grain sizes of the Co-Fe-C alloy films with low CC were obtained using the Debye-Scherrer model [35] as black balls in Fig. 1(c). Both of the SNR and grain sizes analysis in Supplemental Material S1 [25] and Fig. 1(c) revealed that the transition of grain size and lattice disorder was gradual. Moreover, the values of SNR and grain size approached the minimum limits (SNR=1, grain size=2~3 nm [36]) when the CC reached around 4%, suggesting that 4% was a critical CC.

XPS was used to characterize the films' composition because of its high sensitivity to light elements such as boron or carbon. We used the C 1s, Fe 2p and Co 2p peaks of XPS (Supplemental Material S2 [25]) to study the elemental proportions in the films. Here, our $(Co_{0.5}Fe_{0.5})_xC_{1-x}$ films can be expressed as $(Co_xFe_{1-x})_yC_{1-y}$ with x=0.51-0.53 and y=0-0.16 (Supplemental Material S3 [25]). The slight composition deviation can be understood

since the Fe and Co elements on the target surface have different ionization energies and the CC can tune the deposition rate. Moreover, except for the Ar and Ta signal in the XPS survey spectrum (not shown here), no other elements were observed, suggesting the absence of impurities and confirming the high purity of Co-Fe-C alloy films.

To directly observe the films' nanostructure changing with carbon doping, HRTEM was performed in the samples with low, medium and high CC, respectively. Bright field scanning transmission electron microscopy (STEM) imaging and the corresponding energy-dispersive x-ray spectroscopy mapping for each constituent element (Fig. 2(a) and Fig. 2(b)) reveal that Co, Fe and Ta atoms were distributed homogeneously inside each layer region without any segregation at the surface or interface. The straight interfaces between Co-Fe-C film and Ta was distinct as denoted by two yellow dotted lines. Note that the thickness of each layer was 5 nm for under-layer Ta, 20 nm for Co-Fe-C alloy film and 5 nm for capping Ta, respectively, which was consistent with the deposition rates determined by XRR. The HRTEM images of Co-Fe-C films with CC 0% (Fig. 2(d)), 4.4% (Fig. 2(e)) and 13.2% (Fig. 2(f)) were obtained in the same region of each sample denoted by white solid rectangle in low-resolution image in Fig. 2(c). FFT focused on the selected zones (yellow dotted squares, note that only Co-Fe-C was included to avoid confusion from other layers) was performed to observe the nanostructure evolution with carbon doping. As shown in the respective inset of Fig. 2(d)-Fig. 2(f), the transform images changed from diffraction matrix in the CC 0% to a plurality of diffraction rings involving a few dots in the CC 4.4%, and then to weak diffraction in the CC 13.2%. These results verified that the Co-Fe-C films had the ordered lattice at CC 0%, the disordered amorphous at CC 13.2% and the intermediate nanostructure at CC 4.4%.

B. Magnetostriction and piezomagnetic coefficient

Mangetostriction behavior of these Co-Fe-C films is shown in Fig. 3(a) as a function of the in-plane driving magnetic field for Co-Fe-C films with different CC. Samples with CC lower than 4% show no magnetostrictive response until magnetic field reaches more than 30 Oe. With the CC increasing to larger than 4%, the responsive magnetic field to magnetostriction decreases to lower than 20 Oe and then gradually becomes smaller. The magnetostrictive behavior suggests that 4% is a critical CC to separate the films' structure into nanocrystalline and amorphous, which is consistent with the XRD results shown in Fig. 1(c). The λ_s for these Co-Fe-C films are collected as black squares in Fig. 3(b). Interestingly, the λ_s value of the binary $Co_{0.5}Fe_{0.5}$ film is 13 ppm, which is 20% of the reported value 67 ppm [7]. The main reason for this behavior is our use of the small 20 nm thickness samples for magnetostriction measurements, compared to a thickness of 500 nm $Co_{1-x}Fe_x$ films in Ref. [7]. A large thickness is helpful for releasing strain from lattice mismatch and forming magnetic domains and crystal boundaries in the film, leading to the magnetostriction discrepancy in samples with different thickness. The λ_s values firstly increases and reaches a maximum of 75 ppm at CC 5.2%, and then drops to 27 ppm at CC 6.4 %, at last gradually reducing to 10 ppm at CC 15.8%. To ensure the results are repeatable, the magnetostriction, M-H and broadband FMR measurement of the 2nd group of samples fabricated in the same condition were reproduced. The collected information is shown in Fig. S4 [25] for comparison.

To obtain the piezomagnetic coefficient (maximum value of $d\lambda/dH$) of the Co-Fe-C films, magnetostriction constants derive with respect to the in-plane driving magnetic

fields in Fig. 3(c). As shown by the red cycles in Fig. 3(b), a peak in the area with CC between 4% and 6% is observed and biggest value is 10.3 ppm/Oe at 4.8% CC. There have been some reports that the chemical and structural heterogeneity in the oxide and metallic alloy can lead to extraordinary behaviors [7, 37]. So a co-existence phase with CC between 4% to 6% exists in these films is reasonable. We separate the CC into 3 parts, that is, the nanocrystalline *bcc* phase with CC < 4%, amorphous phase with CC > 6% and co-existence phase with CC between 4% to 6%. The phase boundaries are marked with light orange and green dotted lines as shown in Fig. 3(b) and Fig. 3(d). The CC separation here is consistent with the grain size estimation by XRD in Fig. 1(c) and confirmed by FFT analysis in the HRTEM images as shown in Fig. 2. It is believed that the doping metalloid atoms would form atom pairs or clusters that destabilize the parent $D0_3$ phase [38]. Therefore, the CC region 4% to 6% is the optimized concentration for the magnetostriction behavior and piezomagnetic effect for Co-Fe-C films. It should be mentioned that the peak value of λ_s in the Co-Fe-C films is higher than the reported value in Ga-Fe-B films and 3 times higher than the widely used material Co-Fe-B films. Meanwhile, the maximum $d\lambda/dH$ is much larger than other well-known magnetostrictive materials such as Terfenol-D, Ga-Fe-B films and Metglas [39], making these Co-Fe-C films excellent candidates for voltage tunable magnetoelectric devices in multiferroic composite structure.

The ultra-excellent mechanical response induced by electrical and magnetic fields in co-existence phase is universal in the piezoelectric, ferroelectric and magnetic alloy materials [40,37,7]. For the piezoelectric and ferroelectric materials, the local structural heterogeneity triggers the competition between bulk and interfacial energies. The high

mechanical response to the electric field occurs when the impact of interfacial energies is sufficiently large [40,37]. For the magnetic alloy materials, authors thought the phase boundary played a significant role in the enhancement of mechanical response to the magnetic field, which was evidenced in the Fe-Ga alloy system [7]. Therefore, we are believed that this interfacial mechanism is closely related to our co-existence phase sample's results in common. However, the real microscopic origin needs further simulation and first principle calculation.

C. Soft magnetism

Now, we explore the magnetic properties of these Co-Fe-C films. The M-H hysteresis loops (not shown here) scanning between H=+1 and -1 kOe were measured with the field applied along the MEA by the MPMS. The saturation magnetization (M_s) and coercivity (H_c) of each Co-Fe-C film are collected in the Fig. 3(d). As CC increases, the M_s becomes smaller and the entire trend is nearly linear, similar to the results of Co-Fe-B [41] and Ga-Fe-B [22]. The binary $Co_{0.5}Fe_{0.5}$ film has the M_s of 23.5 kG, which is close to what has been reported by Schoen *et al.* [42]. The alloy structure transition with carbon addition does not show obvious influence on the M_s, but the soft magnetism of these films was dramatically improved. The H_c of these Co-Fe-C films is reduced from about 110 Oe for binary $Co_{0.5}Fe_{0.5}$ film to about 10 Oe with CC > 4% and reaches 2 Oe at 15.8%. When the CC is less than 4%, carbon addition cannot totally destroy the *bcc* lattice, but can refine the grain size, resulting in varied H_c. At a CC of 4% or higher, carbon addition destabilize the parent phase, turning Co-Fe-C films from nanocrystalline to amorphous. The elimination of magnetocrystalline anisotropy results in the extremely low

H_c. These changes in soft magnetism are related to the structure transition with carbon addition, which agrees with the previous XRD results. It should be noted that the H_c of the Co-Fe-C films in the nanocrystalline region firstly increases and reaches a maximum of about 180 Oe at CC 1.6 %, and then sharply drops. This result can be understood when combined with the FMR results.

We characterize the magnetic anisotropy of these Co-Fe-C films by VSM in order to obtain further information of the soft magnetism. Because these Co-Fe-C films do not have perpendicular anisotropy (not shown here), large out-of-plane demagnetization field forces the magnetic moments to lie in-plane. A schematic diagram of in-plane magnetic anisotropy measurement obtained from the VSM is shown in the inset of Fig. 4(b). The remanent magnetization ratios (M_r/M_s) along different in-plane directions with 15° or 30° interval were obtained from the M-H loops to show the magnetic anisotropy. Interestingly, an in-plane uniaxial magnetic anisotropy (UMA) was observed in the Co-Fe-C films with CC larger than 4 %, shown as the blue curve in Fig. 4(a), but the films with CC less than 4 % was magnetic isotropy as the orange curve in Fig. 4(a). The M_r/M_s in the UMA can be expressed as: $M_r/M_s = A*\sin^2\varphi+B$, where φ is the angle between applied magnetic field direction and MHA, A and B are the fitting anisotropic coefficients which are varied between 0 and 1. The coefficient A represents the intensity of sample's UMA, as the sample is isotropic with A=0, completely UMA with A=1, and a superposition state of isotropic and UMA with $0<A<1$. Now, the coefficient A of each Co-Fe-C film is collected as black squares in Fig. 4(b). At CC less than 4%, the films are isotropic with A=0. The value for A sharply increases from 0 to 0.8 in the co-existence phase and then gradually decreases in amorphous phase. These films are superposition states with $0<A<1$. The CC-

dependent features of coefficient A have a similar evolution trend with UMA constant (K_u) except in the nanocrystalline *bcc* phase, which will be mentioned later.

The origin of the UMA can be attributed to magnetocrystalline anisotropy, induced anisotropy, interfacial charge transfer and strain effect [43]. We first rule out the induced anisotropy due to the absence of magnetic field during deposition. There have been some reports on the UMA induced by substrate surface topography [44]. However, the silicon (001)-oriented substrate did not show any special topography such as strip or step (not shown here), indicating the UMA is not related in this scenario. The interfacial charge transfer also cannot be the reason of UMA in these films due to the inserted metallic seed layer Ta between substrate and Co-Fe-C films. The thickness of the Ta layer is 5 nm, well above the electric field screening length (1-2 unit cells). Therefore, the UMA could be from the films' magnetocrystalline anisotropy and strain effect. For the films with CC > 6%, UMA from magnetocrystalline anisotropy could be excluded due to its absence in amorphous films. The strain effect from the silicon substrate could be the only reason for the UMA. The under-layer Ta thickness dependent magnetic anisotropy analysis was carried out to further verify the strain effect in Supplemental Material S5 [25]. So far, we believe the residual stress from substrate cutting could contribute to the amorphous films' UMA. For the films with CC <4%, there is a magnetic anisotropy competition between magnetocrystalline anisotropy and strain effect. However, the magnetocrystalline anisotropy is 10 to 100 times larger than the strain effect in these films (detailed calculation are in Supplemental Material S6 [25]), leading the dominant contribution from magnetocrystalline anisotropy. Since these films are polycrystalline here, the magnetocrystalline anisotropy in each grain randomly distribute, making the films

isotropic. It is much more complicated for the films in the co-existence phase. The carbon addition here destroys the *bcc* structure and destabilizes the parent phase. The collapse of the parent structure eliminates the magnetocrystalline anisotropy contribution and brings in the strain effect.

D. Microwave properties

Broadband FMR measurement was carried out with external magnetic field applied parallel to the MEA. The narrow FMR linewidth at X-band (25 Oe in Fig. S7 [25]) was achieved in the sample with CC 4.8%. Fig. 4(c) shows the curves of absorbed linewidth (ΔH) versus resonant frequency (f) with CC ranging from 0% to 15.8%. A linear fitting was applied to each sample using the relation [45]

$$\Delta H(f) = \frac{4\pi\alpha_{tot}}{\gamma} f + \Delta H_0 , \quad (1)$$

where γ is the electron gyromagnetic ratio, α_{tot} is the total Gilbert damping constant and ΔH_0 is the inhomogeneous linewidth broadening at 0 Hz. As shown in the Fig. 4(d), in the nanocrystalline phase, both α_{tot} and ΔH_0 are maximum at CC 1.6%. Then α_{tot} and ΔH_0 sharply decreased to 0.002 and 10 Oe, respectively, when carbon doping reaches the co-existence phase. In the amorphous phase, α_{tot} gradually increased and ΔH_0 decreased with CC increasing. There have been some reports that the in-plane total damping is the sum of the intrinsic and extrinsic damping, where the extrinsic part arises from the spin pumping and two-magnon scattering [46]. But the total extrinsic contribution is about 10^{-3} [45], which will not dominate the CC dependent features in total damping. The minimum α_{tot} here is 0.002, indicating that the minimum of intrinsic damping of these Co-Fe-C films is about 0.001, better than the reported value 0.004 in $Co_{0.4}Fe_{0.4}B_{0.2}$ film [47]. There are only

a limited number of reports for composition analysis of ΔH_0. For Co_xFe_{1-x} alloys, the value of ΔH_0 is related to the amount of defects of the films [48], uniformity of the structure phase [49]. We consider the same factors in these Co-Fe-C films as they have the same parent phase. The relatively large ΔH_0 in the nanocrystalline phase compared to the other phases is caused by the large number of multi-crystal boundaries (a type of structure defects). The sharp decrease of ΔH_0 in the co-existence phase is attributed to the same phase that remains intermixed throughout the transition, but not the segregation near the phase transition as suggested by Schoen *et al.* [49]. The in-plane M_s and K_u can be fitted using [50]:

$$(\omega/\gamma)^2 = (H+2K_u/M_s)(H+4\pi M_s+2K_u/M_s) \quad (2)$$

where Eq. (2) is used when H is applied along MEA in UMA samples. The fitted $\gamma/2\pi$=29.5 ± 1.0 GHz/T is consistent with the reported value [48]. The fitted M_s of samples are shown as the blue open triangles in Fig. 3(d), which agree well with the measured values. The K_u is marked with red circles in Fig. 4(b). Interestingly, the K_u is not 0 in the nanocrystalline phase, different from the previous anisotropic coefficient A's features. It can be understood that anisotropic coefficient A is from M-H loops measurement, representing the macroscopic anisotropy. However, K_u is from resonant field fitting of FMR, representing the intrinsic anisotropy. Based on the strong crystallization evidence in XRD, FFT in HRTEM, relatively large H_c and ΔH_0 in the low CC samples, it is believed that the macroscopic isotropy is due to a random distribution of respective magnetocrystalline anisotropic axis existed in each grain. Hence, the fitted large K_u in the nanocrystalline phase indicates the average magnetocrystalline anisotropy of all grains. Interestingly, the fitted K_u in the low CC samples reach 10^5 erg/cm^3, which is 10 times

more than the value of the amorphous samples. This result is consistent with what we have mentioned in the intensity comparison of magnetocrystalline anisotropy and strain effect. With carbon doping, the magnetocrystalline anisotropy is continuously damaged in the nanocrystalline and co-existence phase, resulting in the sharp decrease of K_u. For the amorphous phase, the magnetocrystalline anisotropy is eliminated and the uniform amorphous proportion enhance with carbon addition, leading to K_u keeping decreasing gradually. The maximum K_u at CC 2% will be discussed later. Thus, K_u is strongly influenced by the alloy structural transition with carbon addition.

E. Thermal stability of magnetic properties

To test the thermal stability of the Co-Fe-C alloy films, three different samples with CC 0%, 4.4% and 13.2% annealed at the same temperature for 1 hour in a continuous Ar gas flow. All samples show the increased M_s with increasing annealing temperature (Fig. 5(a)), the same as the reported results in Co-Fe-B alloy films [51,52] marked by solid balls in Fig. 5(a). Considering the element C and B similarity, this behavior can be understood by the elements interdifussion occurs during the annealing as explained by Wang *et al.* [52]. During the annealing above critical temperature, carbon atoms might diffuse away from Co-Fe-C at interface, resulting in the reduction of magnetic impurities (carbon atoms) and therefore increase the magnetic moment. Since the size of carbon atom is much smaller than the other atoms (Co, Fe and Ta), carbon diffusion must be easier and faster than other atoms, and therefore dominates the magnetization variation during annealing. The net varied M_s is defined as $\triangle 4\pi M_s = 4\pi M_s$ (T)- $4\pi M_s$ (0), where $4\pi M_s$ (0) is the saturated magnetic moment without annealing. The calculated curves are shown in Fig.

5(b), from which one can see all of the three samples are thermally stable up to 250℃. The apparent M_s increase in CC 13.2% and the minimal M_s increase in CC 4.4% are observed at the range of 250℃-500℃. Overall, annealing temperature dependent M_s of Co-Fe-C alloy films show better thermal stability than Co-Fe-B alloy films, which agrees well with the reported works [19,20].

The respective α_{tot} of the three samples after annealing and the corresponding net varied value are displayed in the Fig. 5(c) and Fig. 5(d). Interestingly, the sample with CC 0% shows continuous reduction of α_{tot} in the whole annealing range. The α_{tot} of sample with CC 13.2% is thermally stable up to 300℃, then sharply jumps to high value and finally keeps gradually increasing. These microwave properties change after annealing are consistent with Bilzer's work [53] in the Co-Fe-B alloy films. However, the medium doping sample with CC 4.4% shows the maximum thermal tolerance, from which no apparent alteration of α_{tot} is shown in the whole annealing range. Based on the above discussion, the Co-Fe-C alloy film with co-existence phase is of the best thermal stability among all the samples. It is sure that the varied magnetic properties after annealing depend strongly on the transformation of films' nanostructure. Further investigation is in process to understand the internal mechanism.

F. Electronic structure calculation

Ebert *et al.* [54] and Lounis *et al.* [55] suggested that the intrinsic damping is proportional to the total density of states (DOS) at the Fermi energy ($n(E_f)$) in the breathing Fermi-surface model (as in the case for Co_xFe_{1-x} system [45]). So we performed

electronic structure calculation for Co-Fe-C alloy to gain a deeper understanding of the relation between Gilbert damping and CC. The schematic *bcc* structure of Co-Fe-C alloy is shown in Fig. 6(a). With carbon addition, the local distortion of the positions of Fe or Co atom near the interstitial C atoms can be clearly observed. The periodic cell used for calculation is marked as a dashed line. The detailed description of the calculation method is in Supplemental Material S8 [25]. CC less than 6% is employed in our calculation considering nanocrystalline *bcc* structure. Several representative examples are given in Fig. 6(d). The 3d-states (valley in the DOS below E_f) change obviously, but do not shift with CC increasing. Zooming in on the DOS around E_f (inset of Fig. 6(d)) clearly shows that the CC dependent features in $n(E_f)$ directly correlate to features related to damping as shown in Fig. 6(b). The calculated M_s of each supercell was collected to compare with the measured M_s in Fig. 6(c). The initial increase of $n(E_f)$ with CC < 2% is related to the carbon doping effect on the band splitting of the metal ferromagnetism introduced in the Stoner criterion [6]. This low content doping tunes the magnetic properties of alloys such as H_c, K_u and intrinsic damping as shown in the previous data. Then, $n(E_f)$ decreased with CC > 2%, originated from the strong hybridization between C 2p states and Fe or Co 3d states, which localize the electrons around E_f of the alloy. The extremely low Gilbert damping that we measured is related to the minimum in $n(E_f)$ for CC around 5%, at which the doping of carbon atoms optimally hybridize with surrounding metal Fe or Co atoms [45]. Additional work is being done to investigate the mechanism of the $n(E_f)$ turning point happening at CC around 2%. All the calculation were carried out in the periodic supercell. The unit cell destruction from carbon doping was not considered in the

calculation, which may lead to disagreement between the calculated $n(E_f)$ and M_s with the measured damping and M_s that varies near the structure boundary.

IV. CONCLUSION

In summary, we studied the magnetostriction, soft magnetism and microwave properties of different CC concentrations in $(Co_{0.5}Fe_{0.5})_xC_{1-x}$ films grown on silicon (001) substrates. Three distinct CC regions are identified: below 4% the phase is primarily nanocrystalline *bcc*, above 6% the phase is primarily amorphous, and between 4% and 6% there is mixture of nanocrystalline and amorphous. A combination of high λ_s, high $d\lambda/dH$, low H_c, narrow FMR linewidth, low α_{tot} and high thermal stability have been achieved. The large λ_s and $d\lambda/dH$ was related to the co-existence of nanocrystalline *bcc* and amorphous phase. The extremely low damping was related to the minimum in $n(E_f)$ of the alloys that was inducing by carbon doping. We also analyzed the competition between magnetocrystalline anisotropy and strain effects in determining the magnetic anisotropy of the Co-Fe-C films. This work will stimulate the Co-Fe-C films' application in voltage tunable magnetoelectric devices in multiferroic composite structure and other microwave magnetic devices.

ACKNOWLEDGMENTS

This work was supported by the state scholarship fund of China Scholarship Council (No. 201607285003), National Science Foundation of China (Grant No. 11504327), Zhejiang Provincial Natural Science Foundation of China (Grant Nos. LQ15A040002 and LQ19F010005), Open Project Funding of the Key Laboratory of Electromagnetic Wave

Information Technology and Metrology of Zhejiang Province (Grant No. 2019KF0002), Scientific Research Foundation of Zhejiang University of Technology and in part by the National Science Foundation TANMS ERC Award 1160504. The magnetization work was supported by the National Science Foundation grant ECCS-1402738. The authors wish to thank Dr. S. Zhang for his constructive suggestions and discussions.

[1] C. Chappert, A. Fert, and F. N. V. Dau, The emergence of spin electronics in data storage, Nat. Mater. **6**, 813 (2007).

[2] D. Houssameddine, U. Ebels, B. Delaët, B. Rodmacq, I. Firastrau, F. Ponthenier, M. Brunet, C. Thirion, J.-P. Michel, L. Prejbeanu-Buda, M.-C. Cyrille, O. Redon, and B. Dieny, Spin-torque oscillator using a perpendicular polarizer and a planar free layer, Nat. Mater. **6**, 447 (2007).

[3] T. Maruyama, Y. Shiota, T. Nozaki, K. Ohta, N. Toda, M. Mizuguchi, A. A. Tulapurkar, T. Shinjo, M. Shiraishi, S. Mizukami, Y. Ando, and Y. Suzuki, Large voltage-induced magnetic anisotropy change in a few atomic layers of iron, Nat. Nanotechnol. **4**, 158 (2009).

[4] D. Chiba, S. Fukami, K. Shimamura, N. Ishiwata, K. Kobayashi, and T. Ono, Electrical control of the ferromagnetic phase transition in cobalt at room temperature, Nat. Mater. **10**, 853 (2011).

[5] Y. Kakehashi, Modern Theory of Magnetism in Metals and Alloys (Springer, Berlin, 2012) P. 203-P. 206.

[6] J. M. D. Coey, Magnetism and Magnetic Materials (Cambridge University Press, Cambridge, 2014) P.150-P.152, P. 134-P. 135, P.384-387.

[7] D. Hunter, W. Osborn, K. Wang, N. Kazantseva, J. Hattrick-Simpers, R. Suchoski, R. Takahashi, M. L. Young, A. Mehta, L. A. Bendersky, S. E. Lofland, M. Wuttig, and I. Takeuchi, Giant magnetostriction in annealed $Co_{1-x}Fe_x$ thin-films, Nat. Commun. **2**, 518 (2011).

[8] C. A. Bauer and P. E. Wigen, Spin-wave resonance studies in invar films, Phys. Rev. B **5**, 4516 (1972).

[9] A. J. P. Meyer and G. Asch, Experimental g' and g values of Fe, Co, Ni, and their alloys, J. Appl. Phys. **32**, S330 (1961).

[10] R. A. Reck and D. L. Fry, Orbital and spin magnetization in Fe-Co, Fe-Ni, and Ni-Co, Phys. Rev. **184**, 492 (1969).

[11] D. D. Djayaprawira, K. Tsunekawa, M. Nagai, H. Maehara, S. Yamagata, N. Watanabe, S. Yuasa, Y. Suzuki, and K. Ando, 230% room-temperature magnetoresistance in CoFeB/MgO/CoFeB magnetic tunnel junctions, Appl. Phys. Lett. **86**, 092502 (2005).

[12] S. Yuasa, Y. Suzuki, T. Katayama, and K. Ando, Characterization of growth and crystallization processes in CoFeB/MgO/CoFeB magnetic tunnel junction structure by reflective high-energy electron diffraction, Appl. Phys. Lett. **87**, 242503 (2005).

[13] S. Chikazumi, Physics of Ferromagnetism (Syokabo: Tokyo, 1978) Vol. 1, P. 260.

[14] S. U. Jen, Y. D. Yao, Y. T. Chen, J. M. Wu, C. C. Lee, T. L. Tsai, and Y. C. Chang, Magnetic and electrical properties of amorphous CoFeB films, J. Appl. Phys. **99**, 053701 (2006).

[15] T. Kubota, T. Daibou, M. Oogane, Y. Ando, and T. Miyazaki, Tunneling Spin Polarization and Magnetic Properties of Co-Fe-B Alloys and Their Dependence on Boron Content, Jpn. J. Appl. Phys. **46**, L250 (2007).

[16] S. Ikeda, J. Hayakawa, Y. Ashizawa, Y. M. Lee, K. Miura, H. Hasegawa, M. Tsunoda, F. Matsukura, and H. Ohno, Tunnel magnetoresistance of 604% at 300K by suppression of Ta diffusion in CoFeB/MgO/CoFeB pseudo-spin-valves annealed at high temperature, Appl. Phys. Lett. **93**, 082508 (2008).

[17] T. Kawahara, K. Ito, R. Takemura, and H. Ohno, Spin-transfer torque RAM technology: Review and prospect, Microelectron. Reliab. **52**, 613 (2012).

[18] S. Ikeda, K. Miura, H. Yamamoto, K. Mizunuma, H. D. Gan, M. Endo, S. Kanai, J. Hayakawa, F. Matsukura, and H. Ohno, A perpendicular-anisotropy CoFeB-MgO magnetic tunnel junction, Nat. Mater. **9**, 721 (2010).

[19] A. A. El-Gendy, M. Bertino, D. Clifford, M. Qian, S. N. Khanna, and E. E. Carpenter, Experimental evidence for the formation of $CoFe_2C$ phase with colossal magnetocrystalline-anisotropy, Appl. Phys. Lett. **106**, 213109 (2015).

[20] S. Chen, J. Zhou, W. Lin, J. Yu, R. Guo, F. Poh, D. Shum, and J. Chen, Ferromagnetic alloy material CoFeC with high thermal tolerance in MgO/CoFeC/Pt structure and comparable intrinsic damping factor with CoFeB, J. Phys. D: Appl. Phys. **51**, 055006 (2018).

[21] A. P. Chen, J. D. Burton, E. Y. Tsymbal, Y. P. Feng, and J. Chen, Effects of B and C doping on tunneling magnetoresistance in CoFe/MgO magnetic tunnel junctions, Phys. Rev. B **98**, 045129 (2018).

[22] J. Lou, R. E. Insignares, Z. Cai, K. S. Ziemer, M. Liu, and N. X. Sun, Soft magnetism, magnetostriction, and microwave properties of FeGaB thin films, Appl. Phys. Lett. **91**, 182504 (2007).

[23] P. Li, A. Chen, D. Li, Y. Zhao, S. Zhang, L. Yang, Y. Liu, M. Zhu, H. Zhang, and X. Han, Electric field manipulation of magnetization rotation and tunneling magnetoresistance of magnetic tunnel junctions at room temperature, Adv. Mater. **26**, 4320 (2014).

[24] C. Dong, M. Li, X. Liang, H. Chen, H. Zhou, X. Wang, Y. Gao, M. E. McConney, J. G. Jones, G. J. Brown, B. M. Howe, and N. X. Sun, Characterization of magnetomechanical properties in FeGaB thin films, Appl. Phys. Lett. **113**, 262401 (2018).

[25] See the Supplemental Material at http:// which include Ref. [26-35], for further information concerning XRD analysis, XPS spectra, repeatable measurements for the 2nd group of samples for comparison, under-layer thickness dependent soft magnetism, K_u calculation, narrow linewidth in FMR spectra and description of electronic structure calculation.

[26] J. Stöhr and H. C. Siegmann, Magnetism From Fundamentals to Nanoscale Dynamics, Springer Series in Solid-State Sciences (Springer, Berlin, 2006) P. 385-P. 388.

[27] C. T. Chen,Y. U. Idzerda, H. -J. Lin, N. V. Smith, G. Meigs, E. Chaban, G. H. Ho, E. Pellegrin, and F. Sette, Experimental Confirmation of the X-Ray Magnetic Circular Dichroism Sum Rules for Iron and Cobalt, Phys. Rev. Lett. 75, 152 (1995).

[28] A. S. Aricò, A. K. Shuklab, H. Kimc, S. Parkc, M. Minc, and V. Antonuccia, An XPS study on oxidation states of Pt and its alloys with Co and Cr and its relevance to electroreduction of oxygen, Appl. Surf. Sci. 172, 33 (2001).

[29] C. A. F. Vaz, Electric field control of magnetism in multiferroic heterostructures, J. Phys. Condens. Matter. 24, 333201 (2012).

[30] A. Mardana, S. Ducharme, and S. Adenwalla, Ferroelectric Control of Magnetic Anisotropy, Nano Lett. **11**, 3862 (2011).

[31] G. Kresse and J. Furthmuller, Efficiency of ab-initio total energy calculations for metals and semiconductors using a plane-wave basis set, Comput. Mater. Sci. 6, 15 (1996); Efficient iterative schemes for ab initio total-energy calculations using a plane-wave basis set. Phys. Rev. B 54, 11169 (1996).

[32] J. P. Perdew, K. Burke, and M. Ernzerhof, Generalized Gradient Approximation Made Simple, Phys. Rev. Lett. 77, 3865 (1996).

[33] G. Kresse and D. Joubert, From ultrasoft pseudopotentials to the projector augmented-wave method, Phys. Rev. B 59, 1758 (1999).

[34] H. J. Monkhorst and J. D. Pack, Special points for Brillouin-zone integrations, Phys. Rev. B 13, 5188 (1976).

[35] A. L. Patterson, The Scherrer formula for X-ray particle size determination. Phys. Rev. **56**, 978 (1939).

[36] N. X. Sun and K. Lu, Grain-size limit of polycrystalline materials, Phys. Rev. B **59**, 5987 (1999).

[37] F. Li, D. Lin, Z. Chen, Z. Cheng, J. Wang, C. Li, Z. Xu, Q. Huang, X. Liao, L. -Q. Chen, T. R. Shrout, and S. Zhang, Ultrahigh piezoelectricity in ferroelectric ceramics by design, Nat. Mater. **17**, 349 (2018).

[38] A. E. Clark, J. B. Restorff, M. Wun-Fogle, K. B. Hathaway, T. A. Lograsso, M. Huang, and E. Summers, Magnetostriction of ternary Fe-Ga-X (X=C, V, Cr, Mn, Co, Rh) alloys, J. Appl. Phys. **101**, 09C507 (2007).

[39] J. Lou, M. Liu, D. Reed, Y. Ren, and N. X. Sun, Giant electric field tuning of magnetism in novel multiferroic FeGaB/lead zinc niobate-lead titanate (PZN-PT) heterostructures, Adv. Mater. **21**, 4711 (2009).

[40] J. X. Zhang, B. Xiang, Q. He, J. Seidel, R. J. Zeches, P. Yu, S. Y. Yang, C. H. Wang, Y-H. Chu, L. W. Martin, A. M. Minor and R. Ramesh, Large field-induced strains in a lead-free piezoelectric material, Nat. Nanotechnol. **6**, 98 (2011).

[41] M. Munakata, S. -I. Aoqui, and M. Yagi, B-concentration dependence on anisotropy field of CoFeB thin film for gigahertz frequency use, IEEE Trans. Magn. **41**, 3262 (2005).

[42] M. A. W. Schoen, J. Lucassen, H. T. Nembach, T. J. Silva, B. Koopmans, C. H. Back, and J. M. Shaw, Magnetic properties of ultrathin 3d transition-metal binary alloys. I. Spin and orbital moments, anisotropy, and confirmation of Slater-Pauling behavior, Phys. Rev. B **95**, 134410 (2017).

[43] J. W. Wang, Y. G. Zhao, C. Fan, X. F. Sun, S. Rizwan, S. Zhang, P. S. Li, Z. Lin, Y. J. Yang, W. S. Yan, Z. L. Luo, L. K. Zou, H. L. Liu, Q. P. Chen, X. Zhang, M. H. Zhu, H. Y. Zhang, J. W. Cai, X. F. Han, Z. H. Cheng, C. Gao, D. Xie, and T. L. Ren, Ferroelectric-domain-controlled magnetic anisotropy in $Co_{40}Fe_{40}B_{20}/YMnO_3$ multiferroic heterostructure, Appl. Phys. Lett. **102**, 102906 (2013).

[44] A. Berger, U. Linke, and H. P. Oepen, Symmetry-induced uniaxial anisotropy in ultrathin epitaxial cobalt films grown on Cu (1113), Phys. Rev. Lett. **68**, 839 (1992).

[45] M. A. W. Schoen, D. Thonig, M. L. Schneider, T. J. Silva, H. T. Nembach, O. Eriksson, O. Karis, and J. M. Shaw, Ultra-low magnetic damping of a metallic ferromagnet, Nat. Phys. **12**, 839 (2016).

[46] P. Omelchenko, E. A. Montoya, C. Coutts, B. Heinrich, and E. Girt, Tunable magnetization and damping of sputter-deposited, exchange coupled Py/Fe bilayers, Sci. Rep. **7**, 4861 (2017).

[47] X. Liu, W. Zhang, M. J. Carter, and G. Xiao, Ferromagnetic resonance and damping properties of CoFeB thin films as free layers in MgO-based magnetic tunnel junctions, J. Appl. Phys. **110**, 033910 (2011).

[48] A. J. Lee, J. T. Brangham, Y. Cheng, S. P. White, W. T. Ruane, B. D. Esser, D. W. McComb, P. C. Hammel, and F. Yang, Metallic ferromagnetic films with magnetic damping under $1.4*10^{-3}$, Nat. Commun. **8**, 234 (2017).

[49] M. A. W. Schoen, J. Lucassen, H. T. Nembach, B. Koopmans, T. J. Silva, C. H. Back, and J. M. Shaw, Magnetic properties of ultrathin 3d transition-metal binary alloys. II. Experimental verification of quantitative theories of damping and spin pumping, Phys. Rev. B **95**, 134411 (2017).

[50] O. Kohmoto, Effective demagnetizing factors in ferromagnetic resonance equations, J. Magn. Magn. Mater. **262**, 280 (2003).

[51] T. Liu, Y. Zhang, J. W. Cai, and H. Y. Pan, Thermally robust Mo/CoFeB/MgO trilayers with strong perpendicular magnetic anisotropy, Sci. Rep. **4**, 5895 (2014).

[52] Y. Wang, W. Chen, S. Yang, K. Shen, C. Park, M. Kao, and M. Tsai, Interfacial and annealing effects on magnetic properties of CoFeB thin films, J. Appl. Phys. **99**, 08M307 (2006).

[53] C. Bilzer, T. Devolder, J. V. Kim, G. Counil, C. Chappert, C. Cardoso, and P. P. Freitas, Study of the dynamic magnetic properties of soft CoFeB films, J. Appl. Phys. **100**, 053903 (2006).

[54] H. Ebert, S. Mankovsky, D. Ködderitzsch, and P. J. Kelly, Ab initio calculation of the Gilbert damping parameter via the linear response formalism, Phys. Rev. Lett. **107**, 66603 (2011).

[55] S. Lounis, M. d. S. Dias, and B. Schweflinghaus, Transverse dynamical magnetic susceptibilities from regular static density functional theory: evaluation of damping and g shifts of spin excitation, Phys. Rev. B **91**, 104420 (2015).

FIGURE LEGENDS

FIG. 1. Samples structure and grain size estimation. (a) XRD pattern of $(Co_{0.5}Fe_{0.5})_xC_{1-x}$ films with x = 0 to 5.2%. (b) Rocking curves of the $Co_{0.5}Fe_{0.5}$ (110) reflection. FWHM was obtained using Gauss peak function fitting as dashed curves. Dotted lines are guided to known the FWHM broaden process. (c) FWHM (red balls) and grain sizes (black balls) estimation of samples with CC x = 0 to 5.2%.

FIG. 2. Structure determination via HRTEM. (a) A bright-field STEM image of Ta/CoFeC/Ta/SiO_2/Si (001) substrate. (b) The corresponding energy-dispersive x-ray spectroscopy mappings for Fe, Co and Ta element, respectively. (c) Cross sections of low-resolution TEM with white solid rectangle display the corresponding location of HRTEM. (d)-(f) HRTEM images of Co-Fe-C alloy films with CC 0%, 4.4% and 13.2%, respectively. The FFT of selected zones (yellow dotted squares) are inserted at the bottom left corner.

FIG. 3. Samples magnetostriction and magnetism. (a) Magnetostriction constant of $(Co_{0.5}Fe_{0.5})_xC_{1-x}$ films with x = 0 to 15.8%. (b) The saturated magnetostriction constant (black) and piezomagnetic coefficient (red) with different CC. The structural boundaries of the alloy are marked with light orange and green dotted lines. (c) Piezomagnetic coefficient vs corresponding driving magnetic field for $(Co_{0.5}Fe_{0.5})_xC_{1-x}$ films with x = 0 to 13.2%. (d) The M_s (black) and H_c (red) versus CC. The blue open triangles are the fitted M_s from broadband FMR measurement.

FIG. 4. Samples magnetic anisotropy analysis and Gilbert damping. (a) In-plane angular dependence of M_r/M_s for $(Co_{0.5}Fe_{0.5})_xC_{1-x}$ films with x = 3.3% and 7.1%, respectively. The 0° was along MHA direction. Solid curves are theoretical fittings with sine square function. (b) The collection of UMA coefficients A (black) and fitted UMA constants (red) from Eq. (2) of the Co-Fe-C films. The inset is the side view sketch of in-plane magnetic anisotropy measurement by VSM with magnetic field direction and sample rotation direction. The structural boundaries of the alloy are marked with light orange and green dotted lines as in Fig. 3. (c) Linewidth (symbols) versus frequency for samples with x = 0 to15.8% and fitted to Eq. (1) (solid lines) to determine both Gilbert damping α_{tot} and inhomogeneous linewidth broadening ΔH_0 in (d).

FIG. 5. Thermal stability of Co-Fe-C films with CC 0%, 4.4% and 13.2%. Annealing temperature dependent M_s (a) and α_{tot} (b). The Co-Fe-B alloy films M_s after annealing in the references are collected for comparison as solid balls in (a). The net varied M_s (c) and α_{tot} (d) after annealing.

FIG. 6. DOS calculation for Co-Fe-C films with CC less than 6%. (a) Side view of schematic structure of interstitial C atoms (red balls) in the bulk $Co_{0.5}Fe_{0.5}$ alloy. The radius of C atoms is amplified for clearness. The Fe and Co atoms are represented by gold and blue balls, respectively. The dashed line show the Co-Fe-C supercell employed in our calculation. (b) The measured α_{tot} (black open) and the calculated $n(E_f)$ (red curve). (c)

The comparison of measured M_s (black open) and calculated M_s (red open). The light orange dotted line is the structural boundary as in Fig. 3. (d) Electronic structure of bulk $(Co_{0.5}Fe_{0.5})_xC_{1-x}$ with $x < 6\%$. All alloy compositions are aligned to a common Fermi energy E_f, at zero energy to facilitate comparison. The inset is the DOS zooming in around E_f.

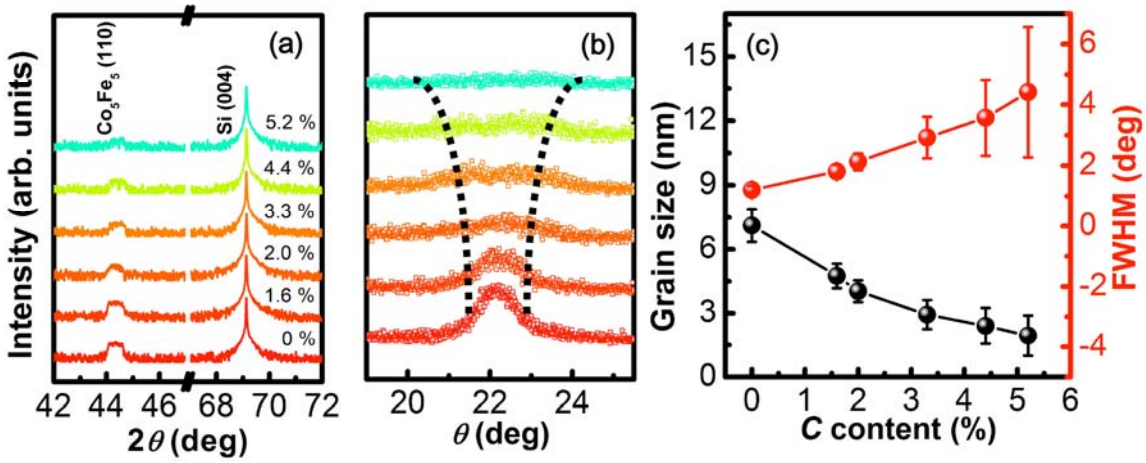
(a)
(b)
(c)
Intensity (arb. units)
Co5Fe5 (110)
Si (004)
5.2 %
4.4 %
3.3 %
2.0 %
1.6 %
0 %
42 44 46 68 70 72
2θ (deg)
20 22 24
θ (deg)
Grain size (nm)
FWHM (deg)
0 1 2 3 4 5 6
C content (%)

Figure 1

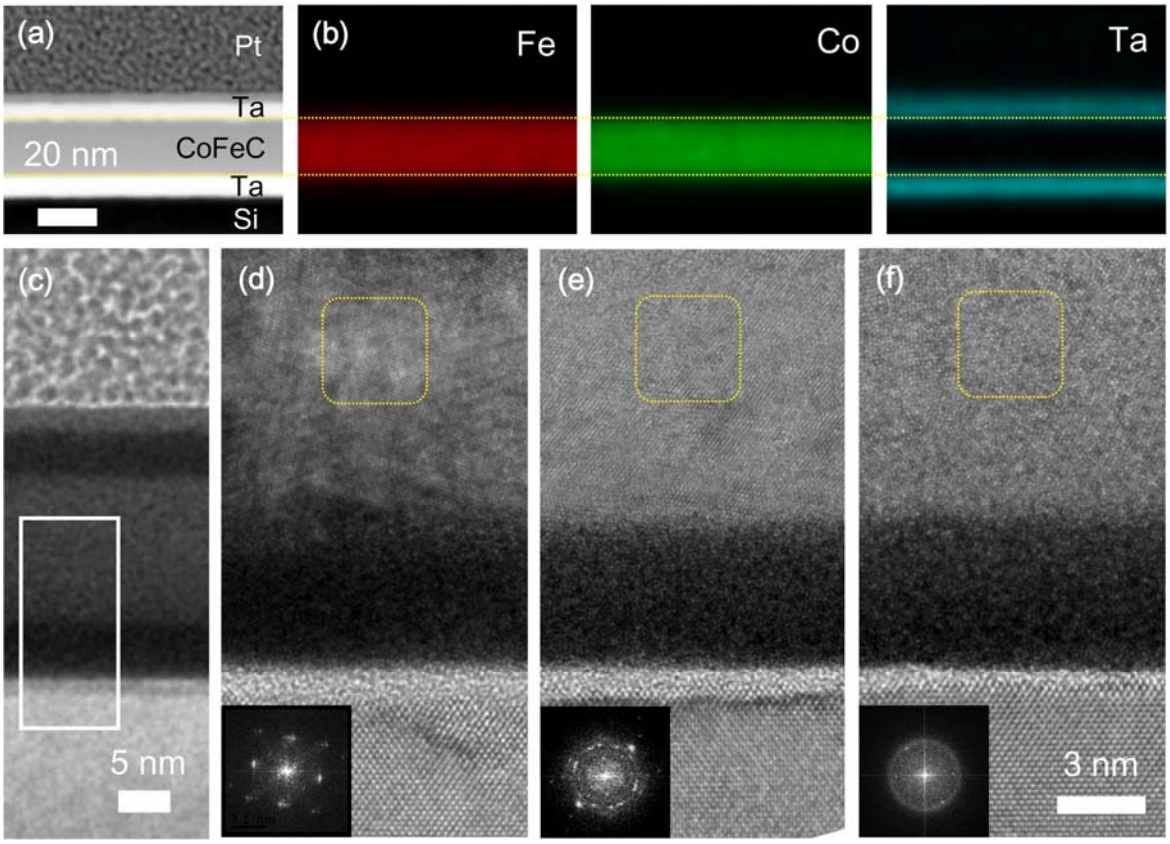

Figure 2

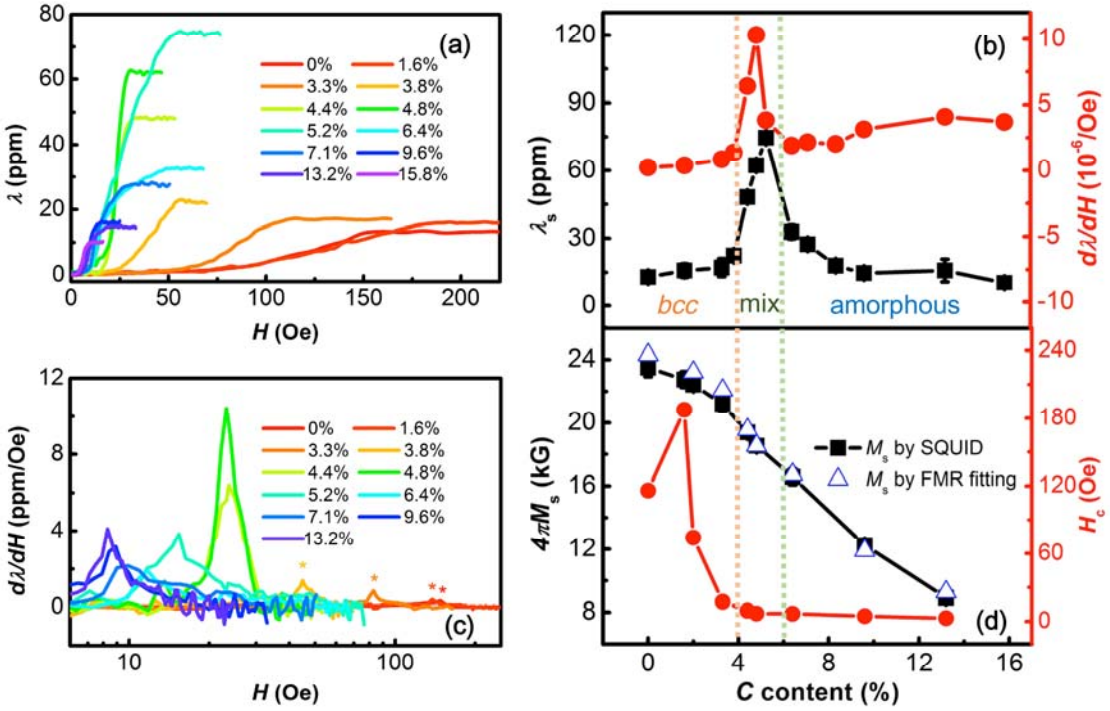
(a)
λ (ppm)
H (Oe)
0%
1.6%
3.3%
3.8%
4.4%
4.8%
5.2%
6.4%
7.1%
9.6%
13.2%
15.8%
(b)
λs (ppm)
dλ/dH (10-6/Oe)
bcc
mix
amorphous
(c)
dλ/dH (ppm/Oe)
H (Oe)
(d)
4πMs (kG)
Hc (Oe)
Ms by SQUID
Ms by FMR fitting
C content (%)

Figure 3

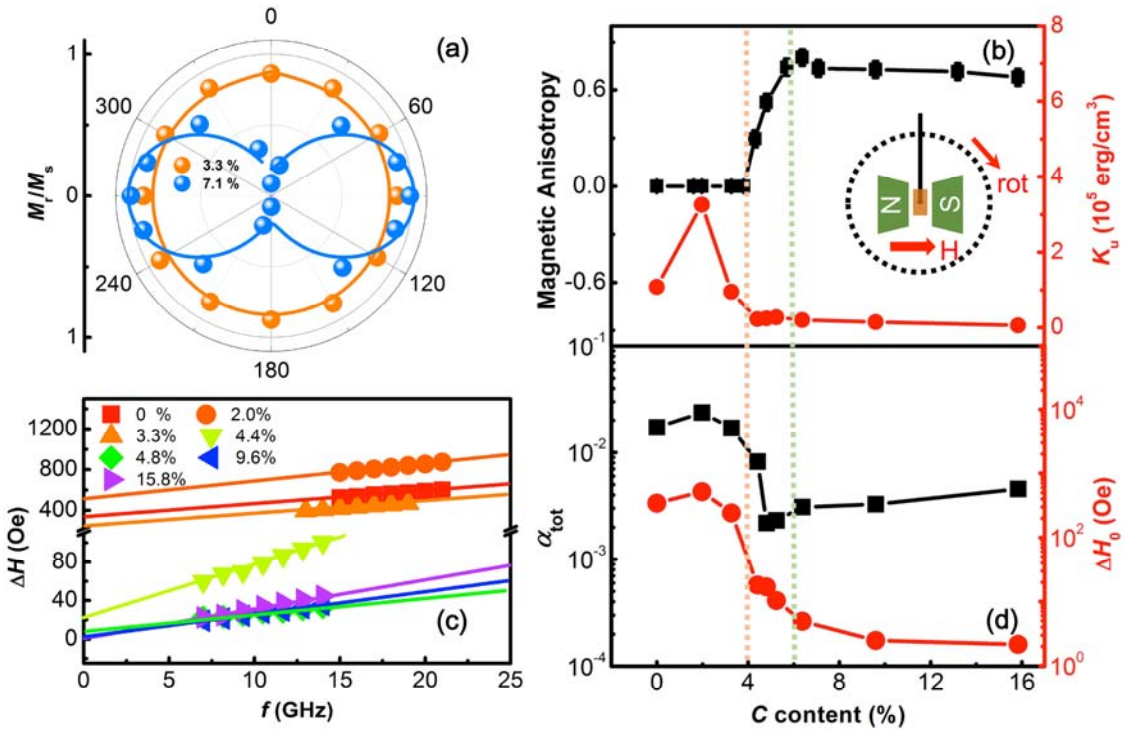
(a)
0
60
120
180
240
300
1
0
1
M_r/M_s
3.3 %
7.1 %
(b)
Magnetic Anisotropy
0.6
0.0
-0.6
10^{-1}
K_u (10^5 erg/cm^3)
8
6
4
2
0
rot
N
S
H
(c)
0 %
2.0%
3.3%
4.4%
4.8%
9.6%
15.8%
1200
800
400
80
40
0
ΔH (Oe)
0
5
10
15
20
25
f (GHz)
(d)
α_{tot}
10^{-2}
10^{-3}
10^{-4}
10^4
10^2
10^0
ΔH_0 (Oe)
0
4
8
12
16
C content (%)

Figure 4

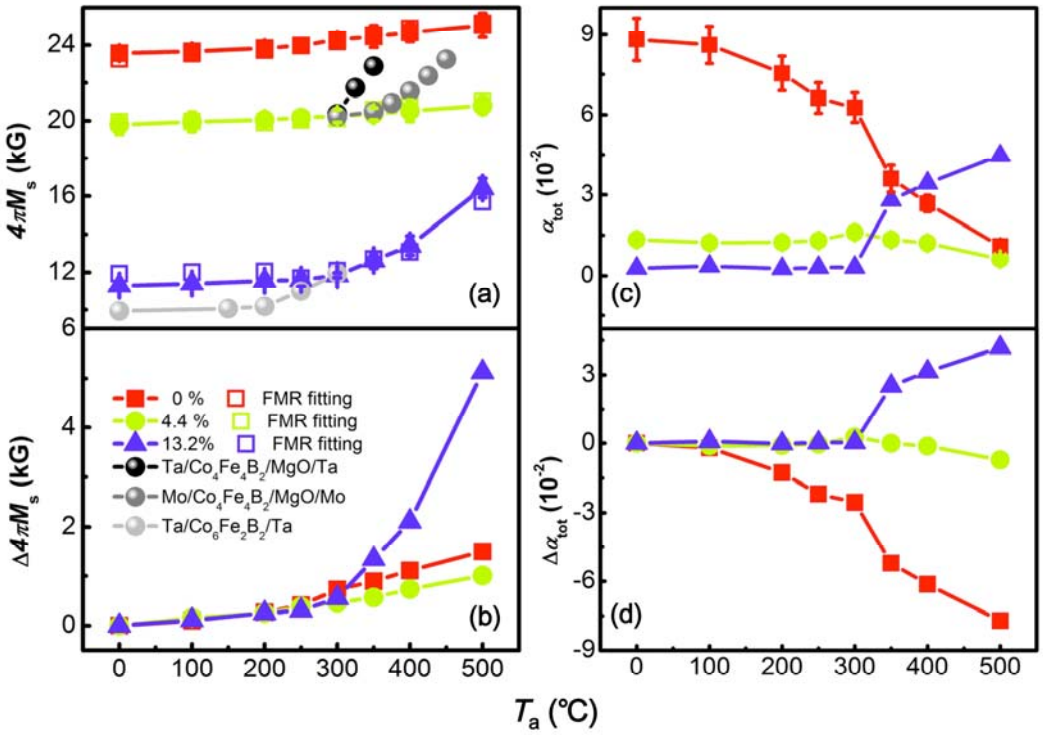
$4\pi M_s$ (kG)
$\Delta 4\pi M_s$ (kG)
α_{tot} (10^{-2})
$\Delta\alpha_{tot}$ (10^{-2})
T_a (°C)
(a)
(b)
(c)
(d)
0 %
4.4 %
13.2%
FMR fitting
FMR fitting
FMR fitting
Ta/Co4Fe4B2/MgO/Ta
Mo/Co4Fe4B2/MgO/Mo
Ta/Co6Fe2B2/Ta

Figure 5

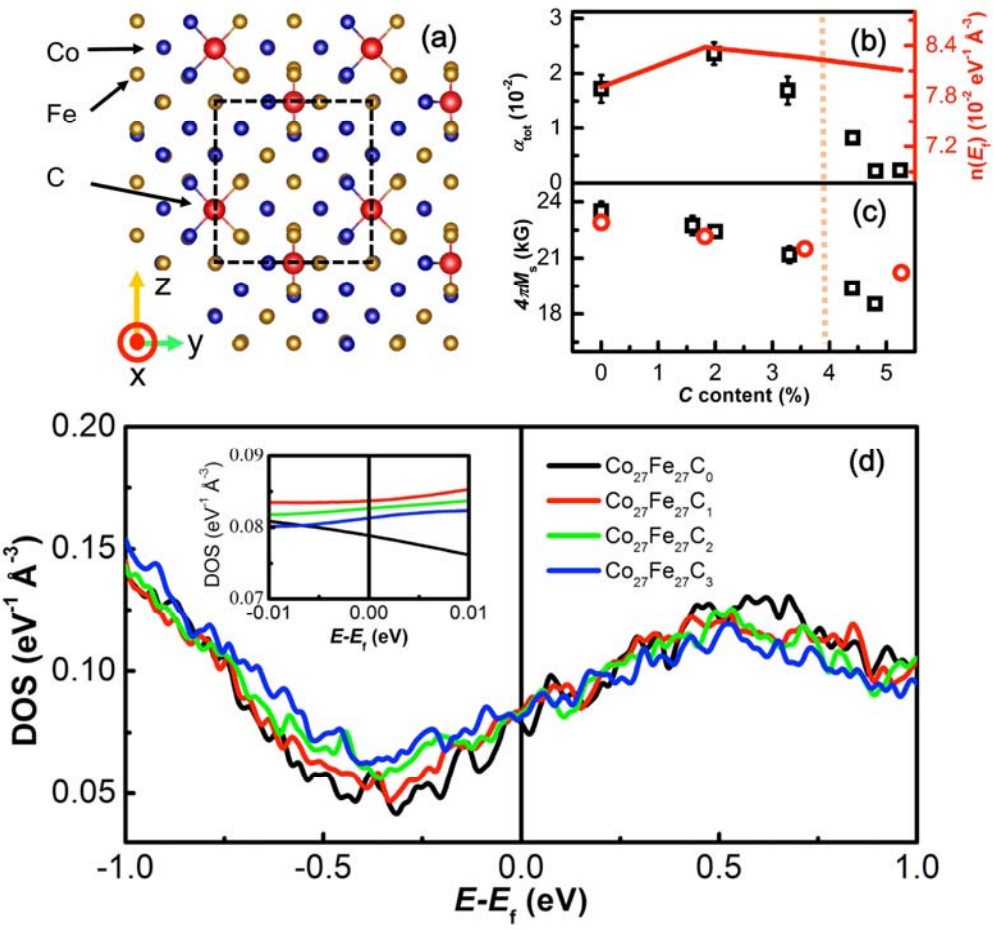
(a)
Co
Fe
C
z
y
x
(b)
(c)
α_{tot} (10^{-2})
$n(E_f)$ (10^{-2} eV^{-1} Å^{-3})
$4\pi M_s$ (kG)
C content (%)
(d)
$Co_{27}Fe_{27}C_0$
$Co_{27}Fe_{27}C_1$
$Co_{27}Fe_{27}C_2$
$Co_{27}Fe_{27}C_3$
DOS (eV^{-1} Å^{-3})
E-E_f (eV)

Figure 6